

Multipartite Quantum Entanglement Evolution in Photosynthetic Complexes

Jing Zhu and Sabre Kais

*Department of Chemistry and Birck Nanotechnology Center,
Purdue University, West Lafayette, IN 47907, USA*

Alán Aspuru-Guzik

*Department of Chemistry and Chemical Biology,
Harvard University, 12 Oxford Street, Cambridge, MA 02138, USA*

Sam Rodriques, Ben Brock and Peter J. Love*

Department of Physics, Haverford College, Haverford, PA 19041

We investigate the evolution of entanglement in the Fenna-Matthew-Olson (FMO) complex based on simulations using the scaled hierarchy equation of motion (HEOM) approach. We examine the role of multipartite entanglement in the FMO complex by direct computation of the convex roof optimization for a number of measures, including some that have not been previously evaluated. We also consider the role of monogamy of entanglement in these simulations. We utilize the fact that the monogamy bounds are saturated in the single exciton subspace. This enables us to compute more measures of entanglement exactly and also to validate the evaluation of the convex roof. We then use direct computation of the convex roof to evaluate measures that are not determined by monogamy. This approach provides a more complete account of the entanglement in these systems than has been available to date. Our results support the hypothesis that multipartite entanglement is maximum primary along the two distinct electronic energy transfer pathways.

I. INTRODUCTION

Photosynthesis is one of the most common phenomena in nature. However, the details of photosynthetic processes are still under investigation. Recent experimental results show

*Corresponding author, plove@haverford.edu

that long lived quantum coherences are present in various photosynthetic complexes [1–3]. One such protein complex, the Fenna-Matthews-Olson (FMO) complex from green sulphur bacteria [4], has attracted a great deal of experimental and theoretical attention due to its intermediate role in energy transport. The FMO complex acts as a molecular wire, transferring the excitation energy from the light-harvesting complex (LHC) to the reaction center (RC) [4–7]. In 2007, Engel et al [8] observed long-lasting quantum beating over a time scale of hundreds of femtoseconds by two-dimensional nonlinear spectroscopy. Evidence for quantum beating, and therefore long lived quantum coherence, was also found at room temperature [9].

The transport of electronic excitations through the protein complex of FMO is an example of energy transport in an open quantum system. The oscillations of the nuclear positions provide a bath or an environment for the electronic excitations. Since 2007, several theoretical frameworks have been developed to model this phenomenon. For example, Aspuru-Guzik et al [10–12] introduced a non-Markov approximation based on the Lindblad formalism to investigate the effects on the efficiency of photosynthesis of the combination of quantum coherence and environmental interaction. Meanwhile, Ishizaki and coworkers [13, 14] utilized the hierarchical equation of motion (HEOM) approach to reproduce the population beating in the FMO complex successfully at both cryogenic and physiological temperature. More recently, Zhu and coworkers [15] introduced the scaled HEOM approach [16] for studying the robustness and quantum coherence in FMO complex. The scaled HEOM approach has been proved to provide a reliable simulation result with considerable reduction in computational requirements. Using the HEOM equations, Rebentrost and Aspuru-Guzik showed that the non-Markovianity of the system is near-maximal at physiological conditions [17]. Recently, many other approaches for the numerical computation of the time evolution and quantum features of this system have made FMO a target for matchmarking of methods for simulating open quantum systems [18–34].

Besides modeling of population and coherence observed in experiment, these models also enable computation of the entanglement evolution [35]. The first study of entanglement in biological excitons was [36], which studied the dynamics of the negativity [37, 38] for a pair of chromophores coupled to a non-Markovian environment. Subsequent studies considered more chromophores, different excitation mechanisms and different entanglement measures. We briefly review this work here, for a more complete overview we refer the reader to a recent review [39]. In a recent study, Mukamel made a distinction between some apparent entanglement effects associated with the linear response which can be eliminated by coor-

ordinates transformation and genuine entanglement that is fundamentally quantum in nature [40]. Recently, Engel et al found a direct evidence of quantum transport in FMO complex [41].

In [42] two measures of entanglement relevant to FMO are defined. The first measure is the concurrence between chromophore i and chromophore j . The concurrence is a well-known measure of entanglement between two two-level systems, and can be computed in closed form even for mixed states, and in the case of a density matrix restricted to the single exciton subspace takes the simple form $C_{ij} = 2|\rho_{ij}|$ [42, 43]. The second measure defined was a global measure related to the relative entropy of entanglement, defined by;

$$E[\rho] = - \sum_{i=1}^N \ln \rho_{ii} - S(\rho) \quad (1)$$

where $S(\rho) = -\text{Tr} \rho \ln \rho$ is the von Neumann entropy of the state ρ . This measure is the relative entropy of entanglement specialized to the case where states only have support in the zero and one exciton subspace. The definition of the relative entropy of entanglement is

$$E[\rho] = \min_{\sigma} \text{Tr}(\rho \ln \rho - \rho \ln \sigma) \quad (2)$$

where the minimization is taken over all separable states σ . In the case of states restricted to zero or one excitons, the set of separable states becomes simply the set of diagonal density matrices, and so this minimization can be performed exactly, yielding the expression (1). We refer the reader to the supplementary materials of [42] for more details. Both of the measures computed in [42] rely on the fact that, in the single exciton subspace, coherence (meaning nonzero off diagonal elements of the density matrix in the standard basis) is necessary and sufficient for entanglement. Both concurrence, the relative entropy of entanglement and an entanglement witness introduced in [42] show this clearly.

We introduce the notation that the bipartite entanglement between subsystems A and B is denoted $A|B$, and when a subsystem consists of a set of chromophores we indicate it by a string of labels, so $12|367$ is the entanglement between the subsystem composed of chromophores one and two (12), and the subsystem composed of chromophores three, six and seven (367).

The two measures considered in [42] are computed for an initial excitation at site one or six, at both $77K$ and $300K$, to probe both physiological conditions and the conditions of ultrafast spectroscopy experiments. For the system initialized with an exciton at site 1, they show the pairwise entanglement $1|2$, $1|3$, $1|5$ and also the pairwise entanglement $3|4$. Finite entanglement was found between all pairs of chromophores in [42] - over distances comparable to the size of the FMO complex - $\leq 30\text{\AA}$.

The logarithmic negativity is the only measure that is readily computable for all states, and in the case of states restricted to the single exciton subspace it may be computed across any cut of the set of seven chromophores into two subsets [44–46]. Caruso *et al.* computed the logarithmic negativity across six cuts 1|234567, 12|34567, 123|4567, 1234|567, 12345|67 and 123456|7 in a simulation in which a single excitation was injected into site one [46]. The entanglement of site one with the rest 1|234567 exhibited the largest peak value, with large oscillations taking it below the entanglements across the other cuts. This may be understood as the generation of entanglement as the delocalization of the injected exciton across the complex. In subsequent work, the logarithmic negativity was also computed (across the same cuts) for simulations in which direct injection of a single exciton is replaced by simulation of thermal injection and laser excitation. In the case of thermal injection the entanglement is reduced by a factor of roughly 50, concomitant with a suppression of coherent oscillations. In the case of simulated laser excitation a large pulse of entanglement is observed, lasting about 0.15 ps.

In [47] Fassioli *et al* move from consideration of the presence of entanglement in models of FMO to characterization of its functional role in transport. It is in this context that the variety of entanglement studies carried out could connect with functionality and delocalization ideas from physical chemistry. Those authors introduce an entanglement yield, based on an entanglement measure which is a sum of the squared concurrences or “tangles” (defined below) over all pairs of chromophores.

$$E_T = \sum_{m,n>m} \tau(\rho_{m,n}) \quad (3)$$

Because of monogamy of entanglement their measure is bounded above by a sum of the tangles of each chromophore with the rest.

$$E_T \leq \frac{1}{2} \sum_n \tau(\rho_n) \quad (4)$$

This upper bound is equal to 2/7 times the Meyer-Wallach measure for the seven chromophore system [48]. In fact it is known that monogamy bounds are saturated in the single exciton manifold [49] and so the measure E_T of Fassioli is in fact exactly equal to 2/7 times the Meyer Wallach Measure. Interestingly, those authors point out a connection of this measure, and hence of the Meyer-Wallach measure, to a measure commonly used by the physical chemistry community of exciton delocalization: the inverse participation ratio [50].

To make a connection between entanglement and transport Fassioli *et al.* [47] define an entanglement yield - the integral of the entanglement (as given by a sum of pairwise tangles)

weighted by the probability density for exciton absorption by the reaction center. This quantity is normalized by the quantum yield: the total probability that the exciton is trapped by the reaction center. The contributions to this quantity were divided into donor-donor, donor-acceptor contributions, where chromophores 1,2 and 5,6 are designated donors and chromophores 3 and 4 are acceptors. This study showed that entanglement peaks on a timescale relevant for transport, for simulations in which the initial exciton is localized on site one or site six. In particular those authors observe an inverse relationship between entanglement among donor sites and quantum efficiency, suggesting that entanglement among the donor chromophores (1,2 and 5,6) may be tuned to achieve the desired quantum efficiency. The authors of [47] also introduce the idea of direct and indirect pathways - an indirect pathway involving transfer through chromophore seven.

In [51] a number of distinct measures of quantum correlation were computed. The quantum mutual information, quantum discord and single-excitation relative entropy of entanglement with respect to bipartite cuts $3|16$, $12|3$ and $3|124567$ were computed. These authors extended the work of [42] by proving a simple formula for the relative entropy of entanglement across any bipartite cut for states restricted to the single exciton subspace.

It is the goal of the present work to further investigate the relationship of multipartite entanglement to the different transport pathways in the context of the HEOM model presented below. The paper is organized as the follows. In Section II the detailed theoretical framework of the scaled HEOM approach is introduced. In Section III the method used to compute the convex roof and hence obtain the entanglement is given. Section IV contains simulation results of multi-partite entanglement evolution. We compute cases where the entanglement can be determined exactly through the monogamy bound in order to validate our convex roof method, and the use the convex-roof optimization to obtain measures that are not determined by the convex roof. We close the paper with some conclusions and directions for future work.

II. METHOD: SCALED HIERARCHICAL EQUATIONS OF MOTION (HEOM)

The structure of the FMO complex was originally analyzed by Fenna and Matthews [4]. The FMO complex consists of three identical monomers arranged in a C3 symmetric structure. Each monomer is formed from seven bacteriochlorophylla (BChla) molecules. These molecules are the “sites” referred to in the rest of the paper. Each monomer works independently in the FMO complex. Experimental results show that site 1 and 6 are close to the light Harvesting complex (LHC) and site 3 and 4 are next to the reaction center

(RC) [4-7].

For all models used in the present paper, the Hamiltonian of the FMO complex and its interaction with the environment is taken to be:

$$\mathcal{H} = \mathcal{H}_S + \mathcal{H}_B + \mathcal{H}_{SB} \quad (5)$$

$$\mathcal{H}_S = \sum_{j=1}^N \varepsilon_j |j\rangle\langle j| + \sum_{j \neq k} J_{jk} (|j\rangle\langle k| + |k\rangle\langle j|) \quad (6)$$

$$\mathcal{H}_B = \sum_{j=1}^N \mathcal{H}_B^j = \sum_{j=1}^N \sum_{\xi=1}^{N_{jB}} \frac{P_{j\xi}^2}{2m_{j\xi}} + \frac{1}{2} m_{j\xi} \omega_{j\xi}^2 x_{j\xi}^2 \quad (7)$$

$$\mathcal{H}_{SB} = \sum_{j=1}^N \mathcal{H}_{SB}^j = - \sum_{j=1}^N |j\rangle\langle j| \cdot \sum_{\xi} c_{j\xi} \cdot x_{j\xi} = - \sum_{j=1}^N \mathcal{V}_j \cdot F_j \quad (8)$$

$$\text{with } \mathcal{V}_j = |j\rangle\langle j| \text{ and } F_j = \sum_{\xi} c_{j\xi} \cdot x_{j\xi}$$

The terms \mathcal{H}_S , \mathcal{H}_B and \mathcal{H}_{SB} describe the Hamiltonian of the system, the bath, and the system-bath coupling respectively. The Hamiltonian is written in the single excitation subspace, so that the basis states $|j\rangle$ in Eq. 6 denotes that the j -th site is in its excited state and all other sites are in their ground states. The energy of site j is denoted by ε_j and J_{jk} is the electronic coupling between site j and k . N is the number of sites, so that $N = 7$ for the FMO complex. For the thermal bath \mathcal{H}_B , the harmonic oscillator model is applied. We assume that each site is coupled to the bath independently. The parameters $m_{j\xi}$, $\omega_{j\xi}$, $P_{j\xi}$ and $x_{j\xi}$ are mass, frequency, momentum and position operator of the harmonic bath associated with the j -th site respectively. The parameter $c_{j\xi}$ in Eq. 8 represents the system-bath coupling constant between the j -th site and ξ -th phonon mode. The system and bath are assumed to be decoupled at $t = 0$.

We can obtain the time evolution of the system density matrix $\rho(t)$ by tracing out the bath degrees of freedom $\rho(t) = \text{Tr}_B [\rho_{tot}(t)] = \text{Tr}_B [e^{-i\mathcal{H}t/\hbar} \rho_{tot}(0) e^{i\mathcal{H}t/\hbar}]$. The correlation function for a phonon bath can be written as

$$C_j(t) = \frac{1}{\pi} \int_{-\infty}^{\infty} d\omega \cdot J_j(\omega) \cdot \frac{e^{-i\omega t}}{1 - e^{-\beta\hbar\omega}} \quad (9)$$

$$J_j(\omega) = \sum_{\xi} \frac{c_{j\xi}^2 \cdot \hbar}{2m_{j\xi} \cdot \omega_{j\xi}} \delta(\omega - \omega_{j\xi}) \quad (10)$$

with $\beta = 1/k_B T$. We assume that $J_j(\omega)$ is the same all sites, $J_j(\omega) = J(\omega) \forall j$ s. We consider the time evolution of the system density matrix both with and without environmental

interaction. For the isolated system, we set $J(\omega) = 0$ and the time evolution of the density matrix for the system is given by:

$$\frac{d}{dt}\rho(t) = -\frac{i}{\hbar}[\mathcal{H}_S, \rho(t)] \quad (11)$$

One approach to the computation of the time evolution of the system density matrix is the hierarchical equation of motion (HEOM) approach, originally developed by Ishizaki and Fleming [14]. We use the scaled HEOM approach for reasons of computational efficiency [15, 16].

In the scaled HEOM approach, the original spectral density function $J(\omega)$ (Eq. 10) is replaced by a Drude spectral density function $J(\omega) = \frac{2\lambda\gamma}{\hbar} \frac{\omega}{\omega^2 + \gamma^2}$ where λ is the reorganization energy and γ is the Drude decay constant. Then the correlation function in Eq. 9 can be expanded as

$$C_j(t > 0) = \sum_{k=0}^{\infty} c_k \cdot e^{-v_k t}$$

with $v_0 = \gamma$, which is the Drude decay constant, $v_k = \frac{2k\pi}{\beta\hbar}$ when $k \geq 1$ and v_k is known as the Matsuraba frequency. The constants c_k are given by

$$\begin{aligned} c_0 &= \frac{\eta\gamma}{2} \left[\cot\left(\frac{\beta\hbar\gamma}{2}\right) - i \right] \\ c_k &= \frac{2\eta\gamma}{\beta\hbar} \cdot \frac{v_k}{v_k^2 - \gamma^2} \text{ for } k \geq 1 \end{aligned}$$

Using the scaled approach developed by Shi and coworkers [16] and applying the Ishizaki-Tanimura truncating scheme [52, 53] to the density matrix, the scaled density operator becomes:

$$\begin{aligned} \frac{d}{dt}\rho_{\mathbf{n}} &= -\frac{i}{\hbar}[\mathcal{H}_S, \rho_{\mathbf{n}}] - \sum_{j=1}^N \sum_{k=0}^K n_{jk} v_k \cdot \rho_{\mathbf{n}} - i \sum_{j=1}^N \sqrt{(n_{jk} + 1) |c_k|} \left[\mathcal{V}_j, \sum_k \rho_{\mathbf{n}_{jk}^+} \right] \\ &\quad - \sum_{j=1}^N \sum_{m=K+1}^{\infty} \frac{c_{jm}}{v_{jm}} \cdot [\mathcal{V}_j, [\mathcal{V}_j, \rho_{\mathbf{n}}]] - i \sum_{j=1}^N \sum_{k=0}^K \sqrt{n_{jk}/|c_k|} \left(c_k \mathcal{V}_j \rho_{\mathbf{n}_{jk}^-} - c_k^* \rho_{\mathbf{n}_{jk}^-} \mathcal{V}_j \right) \quad (12) \end{aligned}$$

where the global index \mathbf{n} denotes a set of nonnegative integers $\mathbf{n} \equiv \{n_1, n_2, \dots, n_N\} = \{\{n_{10}, n_{11}, \dots, n_{1K}\} \cdots \{n_{N0}, n_{N1}, \dots, n_{NK}\}\}$. The symbol \mathbf{n}_{jk}^{\pm} refers to a set in which the number n_{jk} is modified to $n_{jk} \pm 1$ in the global index \mathbf{n} . The sum of n_{jk} is called the tier (\mathcal{N}), $\mathcal{N} = \sum_{j,k} n_{jk}$. The global index \mathbf{n} labels a set of density matrices in which $\rho_{\mathbf{0}} = \rho_{\{0,0,\dots,0\} \cdots \{0,0,\dots,0\}}$ is the system reduced density operator (RDO), and all others are considered as auxiliary density operators (ADOs). Although the RDO is the most

important operator, the ADOs contain corrections to the system-bath interaction, arising from the non-equilibrium treatment of the bath. K is the truncation level for the correlation function (Matsuraba frequency and constant c_k) and the cutoff for the tier of ADOs was set at \mathcal{N}_c . The scaled approach guarantees that all elements in the ADOs decay to zero for the upper levels in the hierarchy, while the Ishizaki-Tanimura truncating scheme decreases the truncation error. For a detailed derivation of this approach we refer the reader to [15]. We make use of the same parameters as [15], and we set the truncation levels $K = 0$ and cutoff tier of ADOs $\mathcal{N}_c = 4$. The reorganization energy and Drude decay constant are $\lambda_j = \lambda = 35 \text{ cm}^{-1}$ and $\gamma_j^{-1} = \gamma^{-1} = 50 \text{ fs}$.

By numerically integrating the differential equation Eq. 12 using Mathematica, we calculated the density matrix of each time step during the evolution for 2500fs with a time step of 2 fs. We performed simulations with two different initial states: site 1 initially excited and site 6 initially excited. The time series of the system density matrix so obtained is the data from which we calculate the entanglement between various different parts of the FMO complex. Before describing the results of those calculations, we first describe the method by which they were obtained.

III. ENTANGLEMENT ANALYSIS

The FMO complex, considered as an assembly of seven chromophores, is a multipartite quantum system. As such, useful information about quantum correlations is obtained by computing the bipartite entanglement across any of the cuts that divide the seven chromophores into two subsystems. Similarly if we take the state of any subsystem of the FMO complex we can compute the entanglement across any cut of the reduced state of that subsystem.

A. Entanglement measures

In the present paper we choose to compute the measures of entanglement defined in [54], which are closely related to previous measures defined by Meyer and Wallach [48], Brennen [55], Scott [56] and Yu and Song [57]. A good starting point for consideration of these entanglement measures is the Meyer-Wallach measure defined in [48]. Given $\rho = |\psi\rangle\langle\psi|$, where $|\psi\rangle \in \mathbb{C}^{2^{\otimes n}}$ with $|\langle\psi|\psi\rangle|^2 = 1$, the Meyer-Wallach measure can be written as fol-

lows [48, 55].

$$Q_{MW}(|\psi\rangle) = \frac{2}{n} \sum_{i=1}^n [1 - \text{Tr}(\rho_i^2)] \quad (13)$$

where ρ_i is the reduced density matrix of the i^{th} qubit.

This measure is based on the fact that the purity or mixedness of the reduced density matrices ρ_i can be viewed as an indicator of entanglement of the i^{th} qubit with the other $n - 1$: $\text{Tr}(\rho_i^2) \leq 1$ such that equality is obtained if and only if ρ is a pure state. We are free to measure entanglement between any pair of subsystems in the same way. We use the set of monotones defined in [54]:

$$\eta_S = \frac{2^{|S|}}{2^{|S|} - 1} (1 - \text{Tr}(\rho_S^2)) \quad (14)$$

where S is a set of k qubits, so that $|S| = k$, and ρ_S is the reduced density matrix over those k qubits.

B. Monogamy of entanglement

A fascinating property distinguishing entanglement from classical correlations is monogamy. Just as the simplest example of entanglement occurs for two qubits, the simplest example of monogamy occurs for three qubits. If, among three qubits ABC , the qubits A and B are maximally entangled, then qubit C cannot be entangled at all with qubits A and B . It is instructive to consider this from the point of view of the entanglement measures (Eq. 13). These measures are based on subsystem purity - if qubits ABC are in a pure state and A and B are maximally entangled then the reduced state of qubits AB is pure, hence so is the reduced state of qubit C , and hence qubit C is unentangled with qubits A and B . In fact, this property extends for three qubits to the case where the entanglement is not maximal. The monogamy constraint is expressed in terms of the tangles measuring the entanglement of qubit A with a subsystem B :

$$\tau_{A|B} = 2(1 - \text{Tr}\rho_A^2) = \eta_A. \quad (15)$$

In terms of the measures (Eq. 15) we obtain:

$$\tau_{A|B} + \tau_{A|C} \leq \tau_{A|BC} \quad (16)$$

This property of three qubit states was shown in [58], and the result for n qubits was proved in [59]:

$$\sum_{i=1, i \neq m}^n \tau_{m|i} \leq \tau(m|1, \dots, m-1, m+1, \dots, n). \quad (17)$$

These imply corresponding relations among the measures η_S that are equal to tangles of one qubit S with the others.

In the context of models of exciton transport that are restricted to the single exciton subspace it is worth recalling that, in the case of pure states of three qubits, it is exactly states that are superpositions of Hamming weight one basis states that saturate the monogamy bound [58]. In fact, for both pure and mixed state cases it has been shown that generalized W states and mixtures of generalized W states with $|0\rangle\langle 0|$ (which corresponds exactly to the case of interest for the single exciton subspace in the models we consider here) saturate the monogamy bounds [49]. We may therefore obtain the entanglement of each chromophore with the rest using the sum of the pairwise entanglements. The other entanglements, of pairs with pairs, and so on, may not be obtained from monogamy properties of qubit W -class states.

It is natural to ask whether monogamy holds beyond restrictions on the entanglement of single qubits to relationships between the entanglement of higher dimensional systems. Unfortunately, this is not the case [60], as it can already be shown that states of qutrits violate the analogous relation to (Eq. 16). However, whether there are other inequalities among the full set of measures η_S is not currently known.

C. Convex Roof Extension of Entanglement Monotones

Given a density matrix ρ and its set of ensemble representations

$$\aleph \equiv \left\{ p_i, |\psi_i\rangle : \sum_i p_i |\psi_i\rangle\langle\psi_i| = \rho \right\}, \quad (18)$$

any entanglement monotone $\eta(|\psi\rangle)$ on pure states can be generalized to a monotone on mixed states, $E(\rho)$, defined by

$$E(\rho) \equiv \inf_{\aleph} \left[\sum_i p_i \eta(|\psi_i\rangle) \right] \quad (19)$$

which is also an entanglement monotone. Given a density matrix $\rho = \sum_i p_i |\psi_i\rangle\langle\psi_i|$, define

$$|\phi_i\rangle\sqrt{q_i} \equiv \sum_j U_{ij} |\psi_j\rangle\sqrt{p_j}, \quad (20)$$

where the U_{ij} 's are elements of a unitary matrix. It can then be shown that $\rho = \sum_i q_i |\phi_i\rangle\langle\phi_i|$.

Since density matrices are hermitian they are always diagonalizable. We can therefore write $\rho = V\Lambda V^\dagger$; this matrix product can equivalently be written as the summation $\rho =$

$\sum_i \lambda_i |v_i\rangle\langle v_i|$, where the λ_i 's are the eigenvalues of Λ and the $|v_i\rangle$'s are the basis-independent orthonormal kets corresponding to the columns of V . This is called the spectral ensemble of ρ . It is also useful to define $\tilde{\Phi} \equiv V\Lambda^{1/2}$, so that $\tilde{\Phi}\tilde{\Phi}^\dagger = \rho$. This object $\tilde{\Phi}$ contains all the information contained in a particular ensemble, and similar objects $\tilde{\Psi}\tilde{\Psi}^\dagger = \rho$ also correspond to ensembles. In fact, the unitary transform given in terms of a summation above corresponds to the matrix transformation $\tilde{\Phi}U$, where U is unitary. If we define $\tilde{\Psi} = \tilde{\Phi}U$ for some unitary matrix U , then $\tilde{\Psi}\tilde{\Psi}^\dagger = \rho$. It can further be shown that the space of ensemble representations of ρ is isomorphic to the unitary group [61]. Hence optimization over the space of ensembles can be reduced to an optimization problem over the unitary group.

D. The Cayley Map

The Cayley map is a self-inverse map from the algebra $u(N)$ to the group $U(N)$. The Cayley map is a map between a number of Lie algebras and their respective groups. It was introduced as a map from $so(N)$ to $SO(N)$ [62]. The Cayley map is defined by

$$\text{Cay}(a) = A = (I - a)(I + a)^{-1} \quad (21)$$

where a is an element of the algebra being considered, and A is an element of the group. Likewise, we have

$$\text{Cay}A = a = (I - A)(I + A)^{-1} \quad (22)$$

In the case of the unitary group, the Cayley map is a bijection between $u(N)$ and the set $U(N) - \mathcal{E}$, where \mathcal{E} is the set of “exceptional elements.” \mathcal{E} is the set of all elements A such that $I + A$ is singular, and can be characterized as the set of all elements A with at least one eigenvalue -1 . The exceptional elements on $SO(3)$ are the reflections. For all such elements E , $I + E$ has a 0 eigenvalue, and is not invertible, so the Cayley map is not defined on these elements; however, this will not hinder our attempts to minimize η over $U(N)$. Since we are performing numerical optimization, we only care that we can get arbitrarily close to a given local optimum. The closure of the image of the Cayley map on $u(N)$ is all of $U(N)$, so we will still be able to identify minima located at exceptional points.

Because $u(N)$ is easily parametrized by N^2 parameters, we can therefore parametrize $U(N)$ by N^2 parameters via the Cayley map. Given a set of N^2 parameters $\{p_1, \dots, p_{N^2}\}$, the corresponding element of $U(N)$ is then:

$$A = \text{Cay}(a(p_1, \dots, p_{N^2})) \quad (23)$$

where a is the element of $u(N)$ given by the parameters p_i under a standard parametrization. In the current work we use the basis of tensor products of Pauli matrices for the algebra $su(N)$. The virtue of the Cayley map is that it gives us an easily understood and easily implemented way to parametrize $U(N)$. The Cayley map thus provides somewhat simpler parameterization than that used in prior work on the convex roof optimization in [63]. Comparison of the performance of our method with the simulated annealing approach described in Appendix B of [64] shows a substantial advantage to parameterization by the Cayley map combined with steepest descent. We leave detailed comparison of our method with that of [63], and the evaluation of other optimization techniques beyond steepest descent, to future work.

IV. RESULTS AND DISCUSSION

There are 63 distinct bipartitions of the 7 chromophores of FMO. Ideally, one would compute all of these measures to obtain a complete picture of the correlations present among subsystems. In practice, one may use the saturation of the monogamy bounds to determine 7 exactly, and the remaining 56 require computation of the convex roof. Instead one may take subsystems and compute the entanglement across bipartitions of the subsystems. For example, by computing the entanglement between all pairs of chromophores. However, as Table I shows, this leads to a large number of subsystems, and a large number of bipartitions for each subsystem. Many of these measures are determined by the monogamy bounds in the single exciton subspace, but not all. In this section, we compute a number of entanglement measures for two, three, four and five qubit subsystems. Our approach follows both that of [42], in which pairwise entanglements were computed, and that of [46] in which the logarithmic negativity for several partitions of the full seven chromophore system were computed. The convex roof optimization described above is necessary, as the results of [42] cannot be extended beyond pairs without it as the optimal ensemble is not known analytically beyond two qubits, and the results of [46] cannot be extended to measures other than logarithmic negativity because other measures do not share the computational tractability of the logarithmic negativity.

A. Two chromophore subsystems

The pairwise entanglements are a natural starting point because they may be computed exactly. For the case in which site 1 was initially excited the coherent oscillations of pop-

m	$\binom{7}{m}$	Cuts	Total Measures	Determined by monogamy	Comment
2	21	1	21	N/A	Can be calculated exactly
3	35	3	105	All	Determined from pairwise entanglements
4	35	7	245	140	$ab cd$, $ac bd$ and $ad bc$ not determined by monogamy
5	21	15	315	105	Ten of fifteen partitions not determined by monogamy
6	7	31	217	42	25 of 31 partitions not determined by monogamy
7	1	63	63	7	Seven determined from pairwise entanglements

Table I: Subsystems and bipartite cuts relevant to the FMO system. One may take a subsystem reduced density matrix of any $m \leq 7$ and consider all the bipartite cuts of each subsystem. This leads to a combinatoric explosion of different bipartite measures. Evidently it would be simpler to consider all cuts of the total system, however, the cost of the convex roof optimization prohibits this at the present time.

ulation occur mainly between sites 1 and 2 before the energy is transferred to sites 3 and 4 [14, 15]. As a result of these coherent oscillations there is large pairwise entanglement between site 1|2 [42]. In the work of [42], for times < 900 (500) fs at 77K (300K) these measures are ordered:

$$1|2 > 1|3 > 1|5 > 3|4 \quad (24)$$

For the system of [42] initialized with a single exciton at site 6 the entanglements 4|5, 4|7, 5|6, 3|4 are computed. For times < 100 fs these are ordered

$$5|6 > 4|5 > 4|7 > 3|4. \quad (25)$$

In Figure 1 we plot the entanglement evolution of the FMO complex when site 1 is initially excited at $T = 77\text{K}$. Figure 1 shows all 21 pairwise concurrences computed by the convex roof. For entanglements 1|2 and 1|3 we also plot the exact concurrence - the agreement is good enough that the difference between the convex roof and the exact calculation is not visible. In Figure 2 we plot the same data when site 6 is initially excited at $T = 77\text{K}$. For entanglements 5|6 and 4|5 we also plot the exact concurrence - again the agreement is good enough that the difference between the convex roof and the exact calculation is not visible. These show the ordering $1|2 > 1|3 > 1|5$ as the significant entanglements for site one initially excited and $5|6 > 4|5$ as the significant entanglements for site 6 initially excited consistent with the results of [42]. Because the monogamy bound is saturated in the single

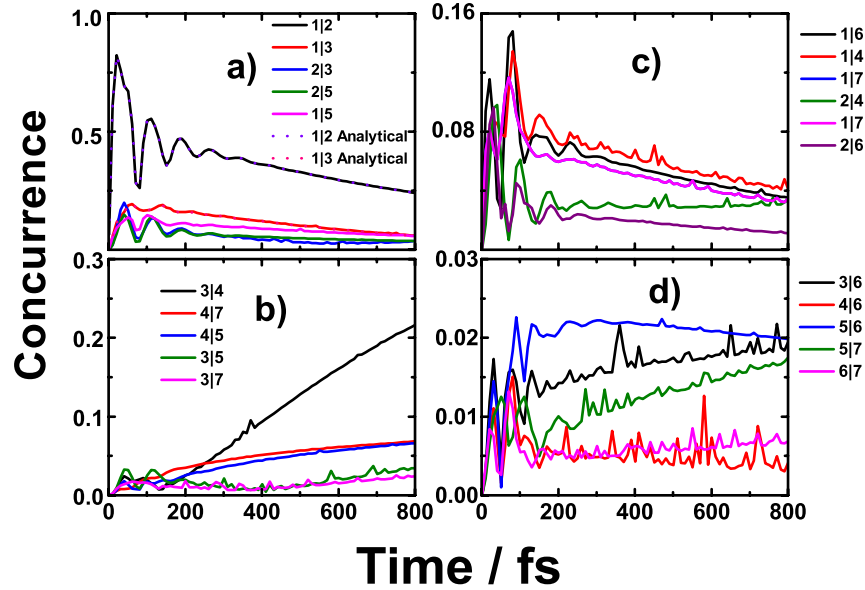


Figure 1: Entanglement evolution in the FMO complex when site 1 is initially excited at $T = 77\text{K}$. This Figure shows all 21 pairwise concurrences computed by the convex roof. For entanglements $1|2$ and $1|3$ we also plot the exact concurrence - the agreement is good enough that the difference between the convex roof and the exact calculation is not visible. Because the monogamy bound is saturated in the single exciton manifold, these 21 measures determine the entanglement of any one chromophore with any subset of the others.

exciton manifold, these 21 measures determine the entanglement of any one chromophore with any subset of the others.

These results on two chromophore subsystems help us identify a pathway involving sites 1234 as significant for exciton transport when site 1 is initially excited, and a pathway involving sites 6543 as significant for exciton transport when site 6 is initially excited. This is consistent with prior results on pairwise entanglement [39, 42]. These results also validate our convex roof computations, at least for the case of two chromophore systems. It is perhaps unsurprising that the convex roof optimization performs well in that setting and so we now turn our attention to larger subsystems.

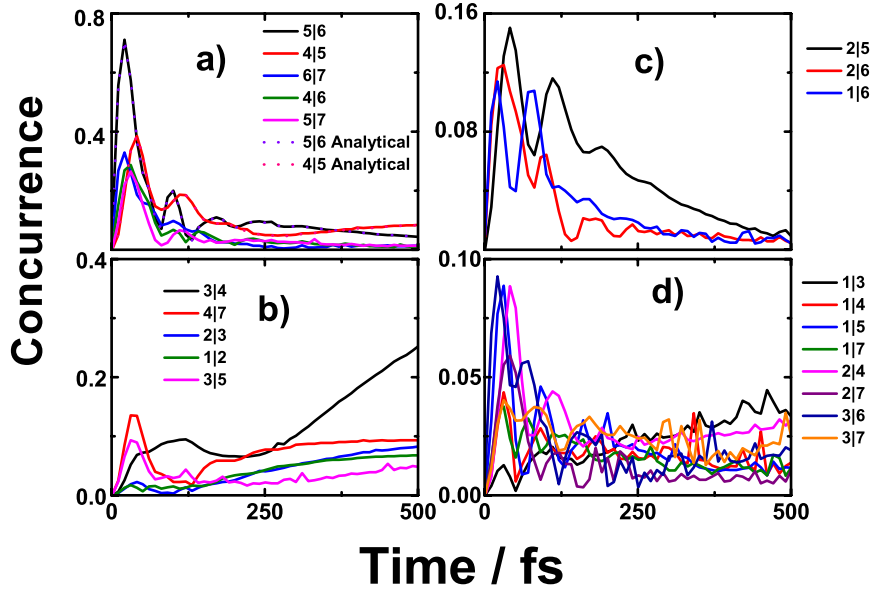


Figure 2: Entanglement evolution in the FMO complex when site 6 is initially excited at $T = 77\text{K}$. This Figure shows all 21 pairwise entanglements computed by the convex roof. For entanglements $5|6$ and $4|5$ we also plot the exact concurrence - the agreement is good enough that the difference between the convex roof and the exact calculation is not visible. Because the monogamy bound is saturated in the single exciton manifold, these 21 measures determine the entanglement of any one chromophore with any subset of the others.

B. Three chromophore subsystems

Figure 3 shows results beyond the pairwise entanglements. We compute the entanglement among the triples 134, 234, 123, 124 both from the monogamy bound and by the convex roof procedure. These results show both the utility of the saturation of the monogamy bound and the performance of the convex roof optimization. We see that the convex roof performs well for three qubits, closely matching the monogamy bound.

Figure 4 shows the triple entanglement evolution among sites 123 in both the isolated system and the system with environmental coupling. The left side of the image shows the entanglement evolution for the isolated system, while the right side is the entanglement evolution under scaled HEOM approach. For the isolated system, the oscillations in population and entanglement will last forever. By comparing it with the open system case, it is obvious

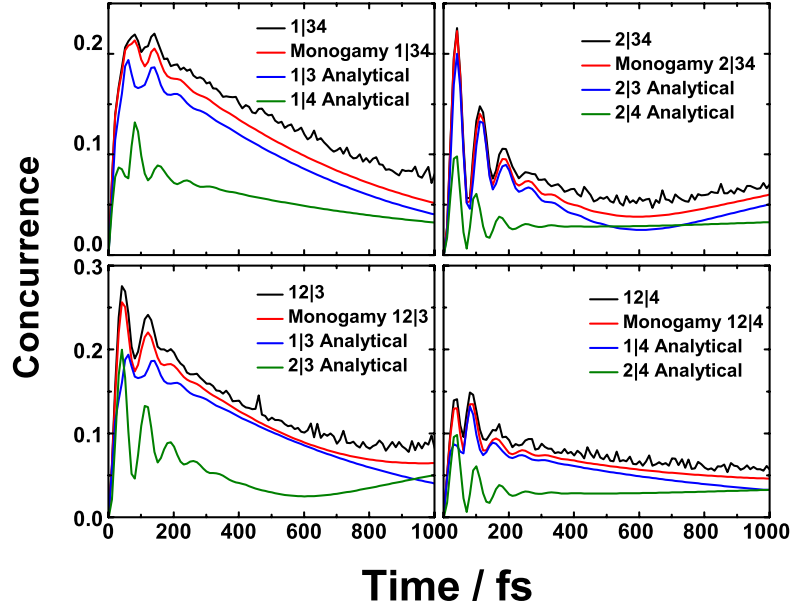


Figure 3: Monogamy bound and convex roof computation of entanglements $1|34$, $2|34$, $12|3$ and $12|4$. Particularly in the first 200 fs the convex roof closely matches the monogamy bound (which is equal to the corresponding tangle due to saturation of the monogamy bounds in the single exciton subspace). These calculations enable us to compute the entanglement among the significant triplets in FMO during transport. They also serve to validate the convex roof code which we shall use to compute entanglements not determined from the pairwise concurrences via monogamy.

that the environment has the effect of eliminating the coherent oscillations characteristic of closed system quantum dynamics. Both isolated and system with environment case hit the maximum and minimum values at the same time during the evolution, which shows that the oscillations in the open system case are indeed the remnants of the coherent behavior in the closed system case. The entanglement evolution is not as smooth as ref. [42], because the simulation data has been sampled every 10fs in order to perform the entanglement calculations.

Fig.4b shows the entanglement of subsystem 123 across partition $1|23$. The pairwise entanglement between site $1|2$ and $1|3$ and the monogamy bound is also shown. Because the monogamy bound is saturated for states in the zero and single exciton subspace [49] these calculations show how well the convex roof optimization is performing. The time series of the triplet entanglement reflects the coherent oscillation of the population and

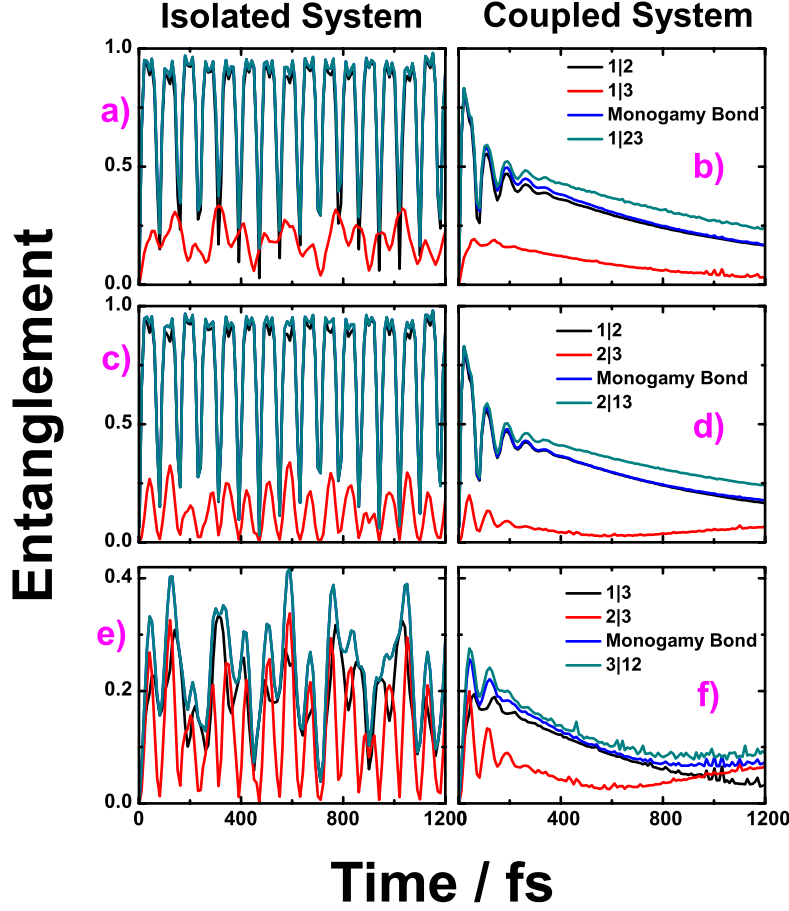


Figure 4: Entanglement evolution of FMO complex when site 1 is initially excited at cryogenic temperature $T = 77\text{K}$. The triplet site entanglement among site 1, 2 and 3 and also the pairwise site entanglement between any two of site 1, 2 and 3 are plotted. The left panel shows the dynamics of the entanglement for the system alone while the right considers the effect of the environment

the time over which these oscillations last is the same as that in the population evolution which is around 650fs. The triplet entanglement evolution is comparable to the pairwise entanglement evolution between site 1|2. In the first a few beating region ($t < 200\text{fs}$), the triplet entanglement is almost the same as that of pairwise site 1|2. Beyond 200fs, the triplet entanglement becomes slightly larger than the pairwise entanglement site 1|2, indicating, via monogamy, that sites one and three have become entangled at this time.

Fig. 4d, shows the entanglement of the triplet 123 across the partition 2|13. This time series is similar to that of 1|23. Another interesting phenomena is the pairwise entanglement

between site 2|3, which also shows coherent oscillations. Although the amplitude of the pairwise entanglement is much smaller compared with the entanglement between site 1|2, they share the same frequency and hit the maximum and minimum value simultaneously.

Fig. 4f shows the entanglement of the triplet 123 across the partition 3|12, which is much smaller than the triplet entanglement 1|23 and 2|13 and does not show significant coherent oscillations. These entanglements are simply sums of pairwise entanglements, by the monogamy bound in the one-exciton subspace. For this case, in which site 1 is initially excited, the dominant pairwise entanglement is 1|2, which is consistent with the other results in the literature [42, 45, 46].

As a result, we conclude that in this pathway: during the coherent evolution period (first 200fs), sites 3 and 4 are competing with each other to be entangled with site 12. However, when the coherent evolution disappears, the entanglement between site 3 and 4 becomes dominant.

In order to check the thermal effect for the entanglement evolution, we plotted the entanglement evolution under room temperature ($T = 300\text{K}$) for both site 1 and site 6 initially excited. By comparing with the evolution at $T = 77\text{K}$, the coherent oscillations were reduced from 4 to 2 oscillations and the length of coherent oscillations was also reduced from 650fs to 400fs. The maximum entanglement during the evolution was also reduced due to the increase in temperature. For example, the maximum triple entanglement of site 1|23 is 0.85 at 77K while that is around 0.73 when $T = 300\text{K}$. In addition the entanglement goes to the equilibrium state much faster at 300K than at $T = 77\text{K}$. It takes around 7ps for the system to arrive at the equilibrium state at $T = 77\text{K}$, while at $T = 300\text{K}$ this takes around 1.5ps. The results at 300K are shown in Figure 5.

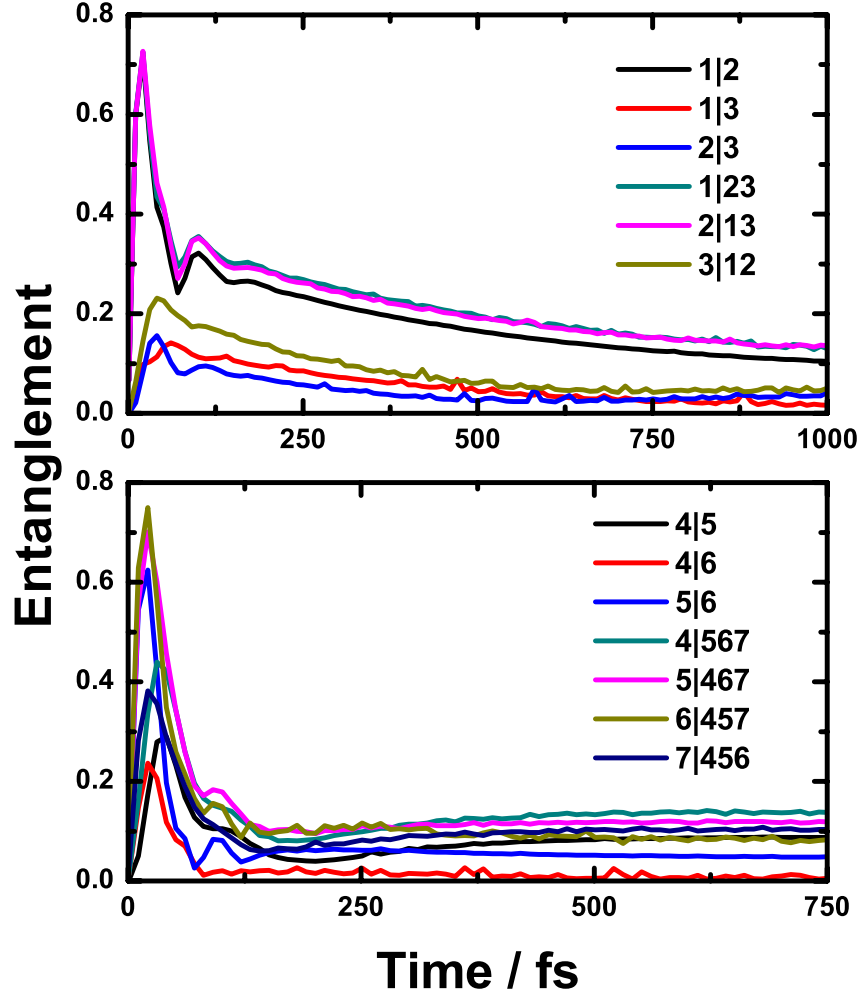


Figure 5: Time evolution of entanglement for multiple sites at $T = 300\text{K}$). The upper panel shows the entanglement when site 1 initially excited. Both triplet and pairwise sites entanglement among site 1, 2 and 3 are plotted. For the lower panel, site 6 is initially excited. We are focus on the quadruplet and pairwise entanglement among site 4 – 7.

C. Four qubit subsystems

Once again, for four qubit subsystems we may use the monogamy bounds to evaluate the performance of our convex roof calculations.

In Figure 6 we evaluate the performance of our convex roof optimization using the monogamy bounds. As one can see, the agreement is less good than for two and three chromophore systems, but is significantly better in the case where the entanglements are

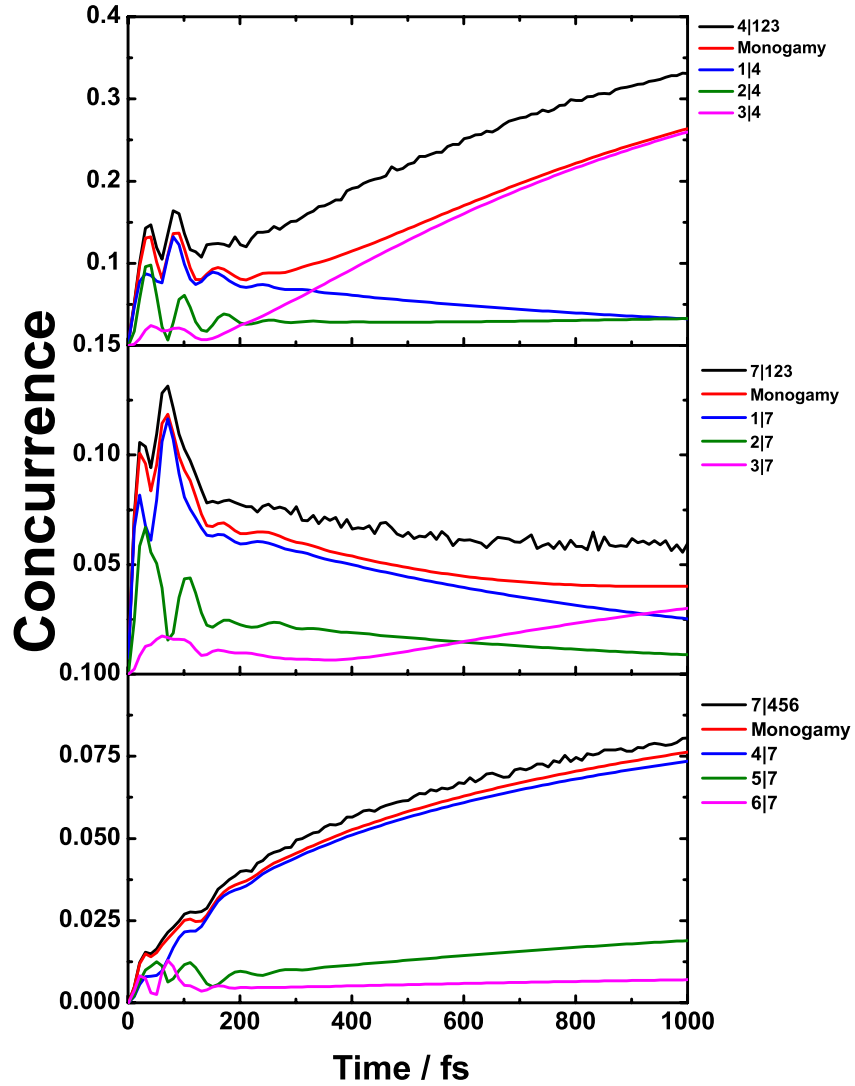


Figure 6: Entanglements in a four qubit system and monogamy bounds when site 1 is initially excited at temperature $T = 77\text{K}$. The entanglements $4|123$, $7|123$ and $7|456$ are shown here - both computed exactly using the monogamy bound and determined by the convex roof. We see a larger variation in performance of the convex roof optimization here, with better agreement for $7|456$ and $7|123$ than for $4|123$.

rather small.

Next we examine the different roles of sites 3 and 4 in the pathway identified above for the case where site 1 is initially excited. It is known that the destination of this pathway is

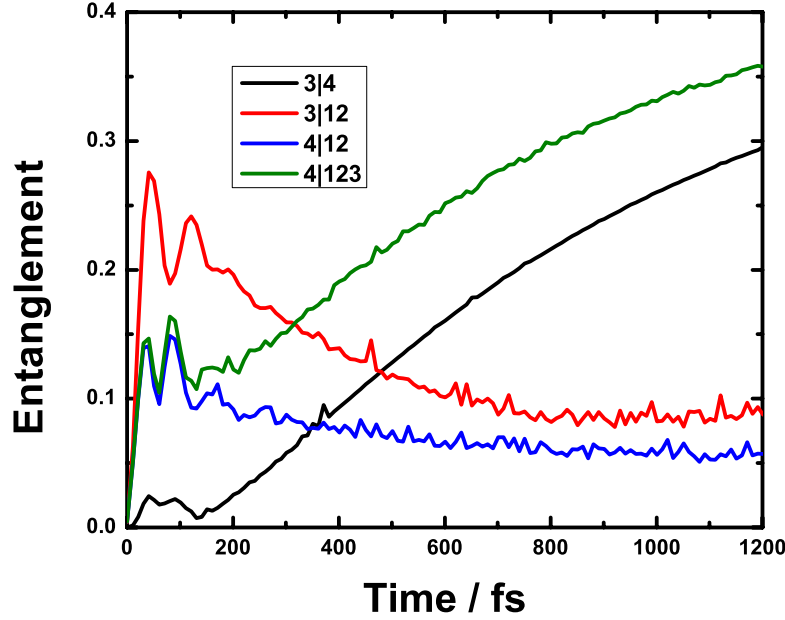


Figure 7: Time evolution of entanglement related to site 3 and 4 for site 1 initially excited under $T = 77\text{K}$. Biparticle (site 3|4) triplet-particle (3|12; 4|12) and quadruplet-particle (4|123) are all considered here.

the pair of sites 34. However, the detailed roles of these two sites during the entanglement evolution is still not clear. Figure 7 shows the entanglement evolution of the quadruple 1234 across partition 4|123. It is clear that the pairwise entanglement 3|4 evolves in lockstep with 4|123 after 200fs. The entanglement of 3|12 and 4|12 are also evolving comparably after 200fs. Within the first 200 fs we see coherent oscillations in which 3|12 and 4|12 are in antiphase, but where 4|123 is in phase with 4|12. This behavior is suggestive of an initial period (the first 200 fs) in which the entanglement of chromophore 4 with 123 is fixed by its entanglement with chromophores 12, and then a long - time behavior in which chromophore 4 is entangled with chromophore 3. This is consistent with a picture of energy transport in which a delocalized exciton passes from chromophores 12 to chromophores 34 - eventually landing at chromophore 3.

In Figure 8 we compute the entanglement between pairs of chromophores 12 and 34 for the case where site 1 is initially excited. These entanglements are not bound by monogamy. Comparison of this figure with Figure 7 is instructive, as we see that the entanglement between the pairs of chromophores 12 and 34 is decreasing after the first 200 fs - following the falling entanglement of the pair 1|3. This makes sense in a picture of transport in which

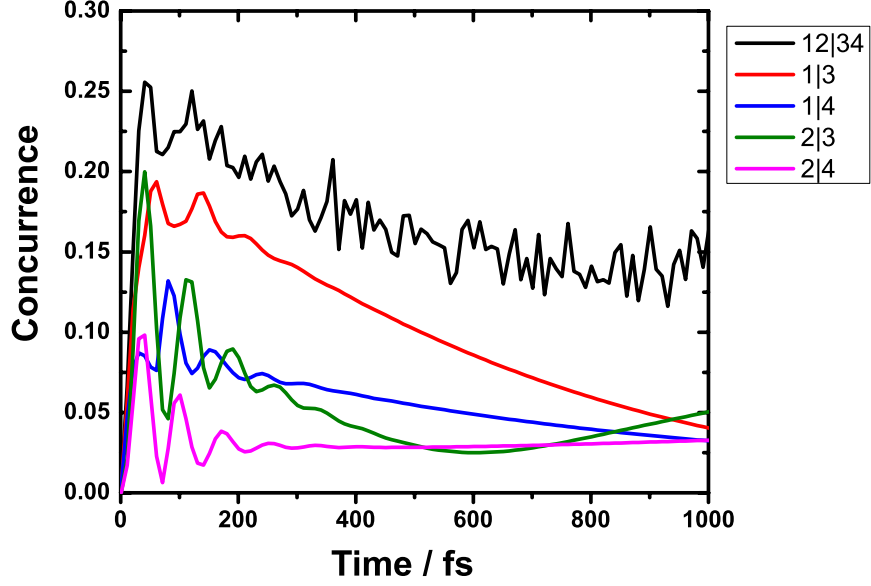


Figure 8: Entanglements in a four qubit system when site 1 is initially excited at temperature $T = 77\text{K}$. The entanglement $12|34$ computed via the convex roof procedure is shown here, together with the significant pairwise entanglements (computed exactly) among the quadruple. Although monogamy bounds do not apply in this case (as neither of the subsystems 12 or 34 is a qubit), we see that the entanglement $12|34$ evolves similarly to the $1|3$ entanglement.

12 are the chromophores receiving the exciton when it is injected and 34 receive the exciton before it passes to the reaction center.

For the case in which site 6 is initially excited, we compute entanglement among significant quadruplets of sites. Fig. 9 shows the entanglement evolution of the quadruplet 4567 for both the isolated and the open system case. Similar to the case where site 1 is initially excited, the entanglement displays coherent oscillations. Furthermore, these oscillations persist as long as the oscillations in the population. However, the timescale over which these coherent oscillations last is only 300fs, much shorter than the case where site 1 is initially excited. This phenomena is consistent with the population evolution [14, 15]. The most significant pairwise entanglement is $5|6$, for which the maximum value can go as high as 0.8. The second most important pairs are sites $4|5$ and $4|6$, which have the maximum amplitude around 0.4. On the other hand, the coherent oscillations for all three pairs share the same frequency and evolution trend besides the 1st beating. The quadruplet entanglement $6|457$ and $5|467$ have similar amplitude and evolution process, while the quadruplet $3|567$ and

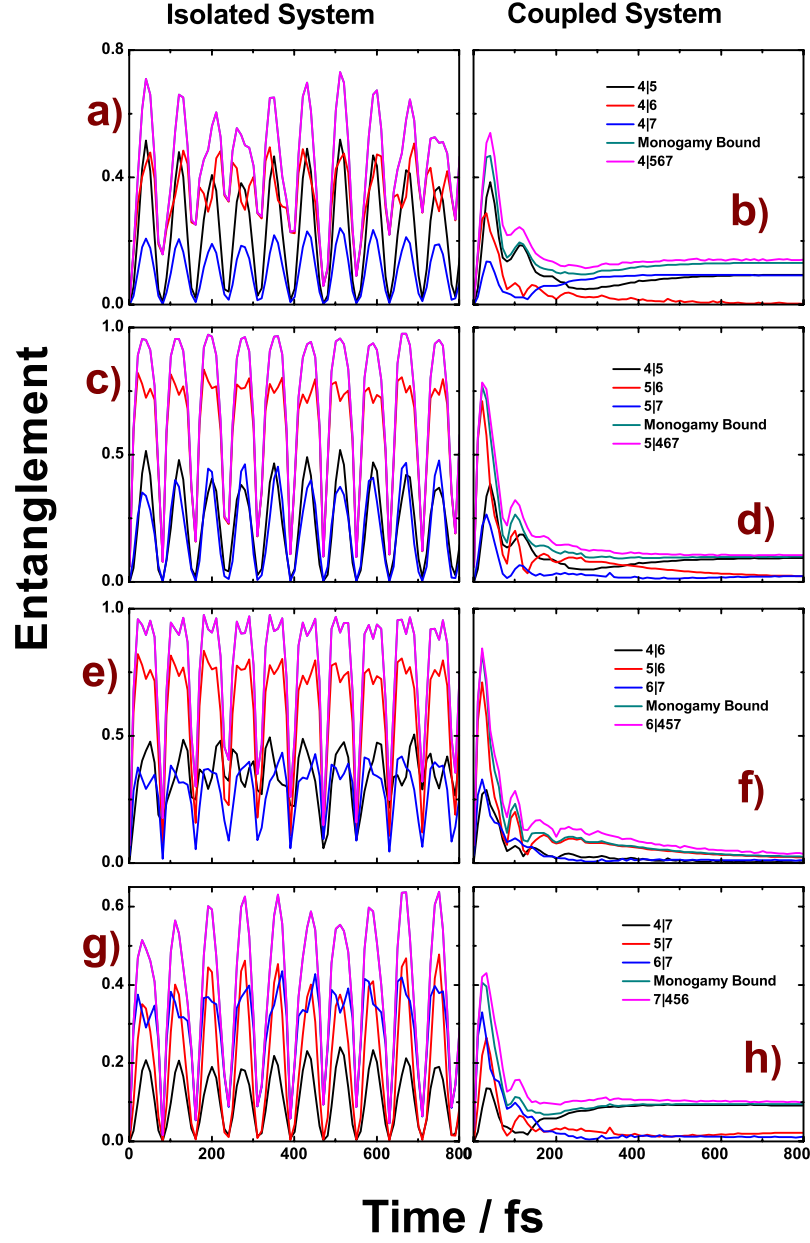


Figure 9: Entanglement evolution of FMO complex when site 6 is initially excited at temperature $T = 77\text{K}$. The quadruplet sites entanglement for site 4 – 7 and the bi-site entanglement between each two sites among them are plotted. The left panel shows the isolated situation and the right panel considers the dynamics with environment.

4|567 are much smaller compared with the above two. During the first two beatings, the triplet entanglement is almost the same as the pairwise entanglement. This shows again that the triplet entanglement under this initial condition is still dominated by the pairwise entanglement - consistent with the saturation of monogamy bounds in this case.

D. Five qubit subsystems

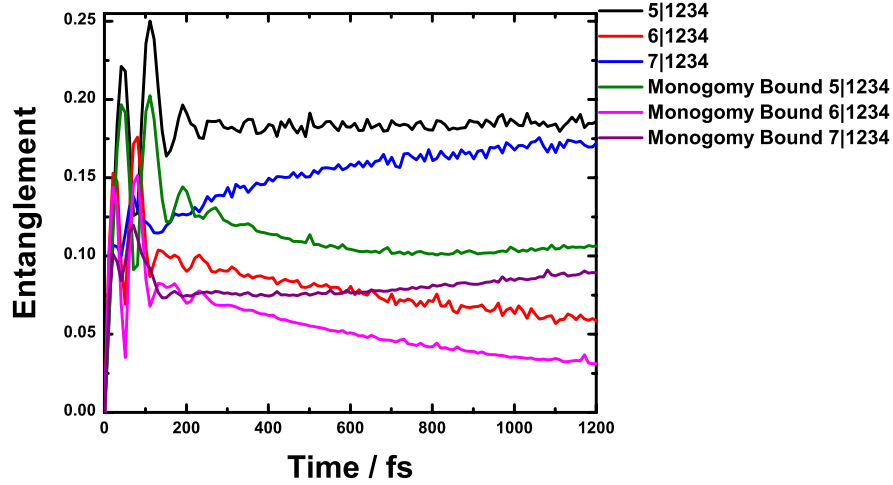


Figure 10: Entanglement evolution of the quintuplet sites (5|1234, 6|1234 and 7|1234) and the corresponding monogamy bounds in the FMO complex under the cryogenic temperature $T = 77\text{K}$. Site 1 is initially excited. Site 1, 2, 3 and 4 are sites evolved in the population pathway under this initial condition.

Fig. 10 shows the quintuplet entanglement evolution among site 5, 6 and 7 with quadruplet sites 1234. All three combinations 5|1234, 6|1234 and 7|1234 have very small entanglement during the time evolution. For the case in which site 1 is initially excited, the entanglement evolution only happens among sites in the pathway, which is site 1, 2, 3 and 4. We also plotted the monogamy bounds in Fig. 10, which indicates the monogamy bounds are always smaller than the corresponding quintuplet entanglements - this shows that, unsurprisingly, the convex roof optimization is not performing as well in the five qubit case as it does for three and four qubits.

For the case in which site 1 is initially excited, entanglement is only significant within the sites in the pathway. We would like to know if this is also the case when site 6 is initially excited. Figure 11 shows the quintuplet entanglement for sites 1 and 2 with sites 4567.

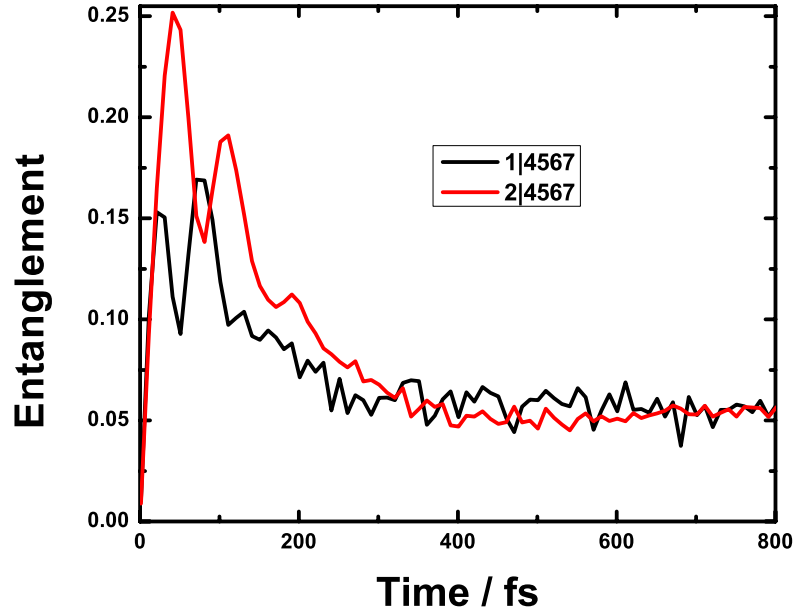


Figure 11: Time evolution of entanglement among five-site 1|4567 and 2|4567 in the FMO complex for site 6 initially excited situation. The system is under cryogenic temperature 77K

The maximum entanglement for those 2 is around 0.25, which is much smaller compared with that among quadruplet sites 4567. This is consistent with the idea that entanglement is concentrated among the sites evolved in a specific pathway, with different pathways for different initial conditions.

As for the site 1 initially excited case, we also examined the roles of sites 3 and 4 in the case when site 6 is initially excited (Fig. 12). Just as in the case where sit 1 was initially excited (Figure 7) we see a 200fs period with coherent oscillations in the entanglement in which the entanglement of 3 with the rest and 4 with the rest are in antiphase. This is followed by a later period in which sites 3 and 4 become entangled and the entanglement of 3 with 4567 is dominated by the entanglement of 3 and 4. As a result, the dominant pairwise entanglement changes from site 5|6 to pair 3|4 during the transport of the exciton from the injection site at site 6 to the final state in which it is concentrated on sites 3 and 4.

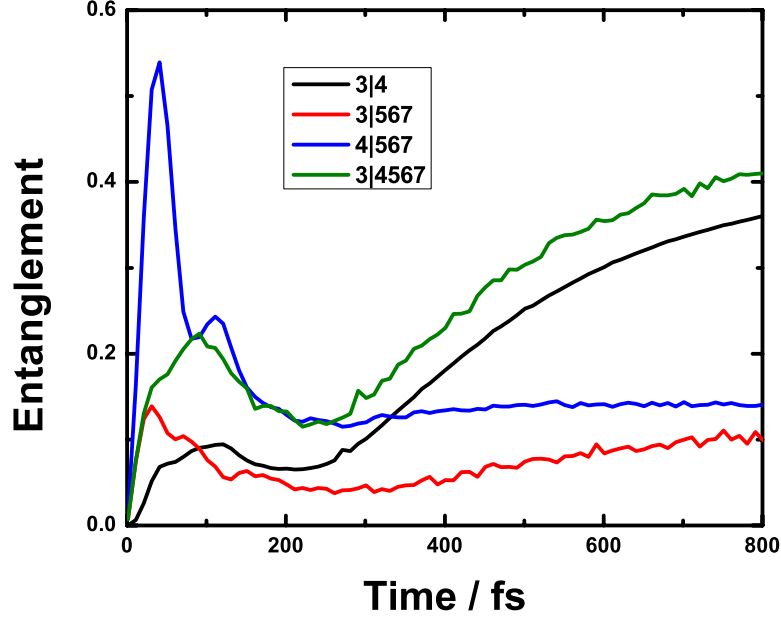


Figure 12: Similar to Figure 7, the entanglement evolution related to site 3 and 4 are investigated when site 6 is initially excited. The entanglement of site 3 and 4 with the other three sites 5, 6 and 7 is considered

E. Beyond the single exciton manifold

In addition to measuring entanglement in the one-exciton subspace, we conducted a number of tests where we manually reinserted the ground state density matrix $\rho_0 = |0000000\rangle\langle 0000000|$ and the two-exciton density matrix $\rho_2 = |0000011\rangle\langle 0000011|$ in order to try to determine how the entanglement would be affected. In the first test, we inserted the ground state ρ_0 on its own, yielding the following expression for the density matrix (where ρ_1 is the density matrix for the single-exciton subspace):

$$\rho = \frac{\rho_0 + |\alpha|^2 \rho_1}{1 + |\alpha|^2} \quad (26)$$

In our second test, we added in the two-exciton subspace alone, without the ground state:

$$\rho = \frac{\rho_1 + |\alpha|^2/2 \rho_2}{1 + |\alpha|^2/2} \quad (27)$$

We then inserted ρ_0 and ρ_2 as follows:

$$\rho = \frac{\rho_0 + |\alpha|^2 \rho_1 + |\alpha|^4/2 \rho_2}{1 + |\alpha|^2 + |\alpha|^4/2} \quad (28)$$

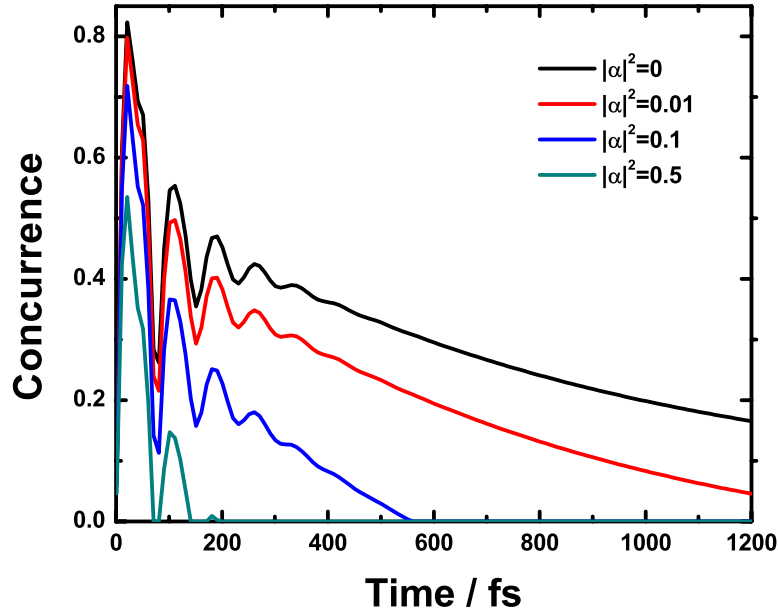


Figure 13: A comparison of the effects of adding in the two-exciton subspace for different values of $|\alpha^2|$. The entanglement between sites one and two is plotted for the density matrix in equation 27, with $|\alpha^2| = .5, .1, .01$.

When we added in both the vacuum state and the two-exciton subspace $|0000011\rangle\langle 0000011|$ and varied α , we found that for values as small as $|\alpha|^2 = .01$, the entanglement completely disappeared. We then experimented with adding in both the ground state and an exponentially decaying two-exciton subspace, $\rho_2 = e^{-\gamma t}|0000011\rangle\langle 0000011|$, and, as expected, as $e^{-\gamma t}$ goes to zero, we recover some entanglement between sites 1 and 2, although the magnitude is still diminished by the presence of the vacuum state 29. In order to get a sense of how quickly the entanglement recovers, we calculated the concurrence for the density matrix in equation 28, which includes the ground state $|0000000\rangle\langle 0000000|$ and the two-exciton subspace $|0000011\rangle\langle 0000011|$ scaled by a factor $\gamma \in [0, 1]$:

$$\rho = \frac{\rho_0 + |\alpha|^2 \rho_1 + \gamma |\alpha|^4 / 2 \rho_2}{1 + |\alpha|^2 + \gamma |\alpha|^4 / 2} \quad (29)$$

The results are plotted in Figs. 14 and 15.

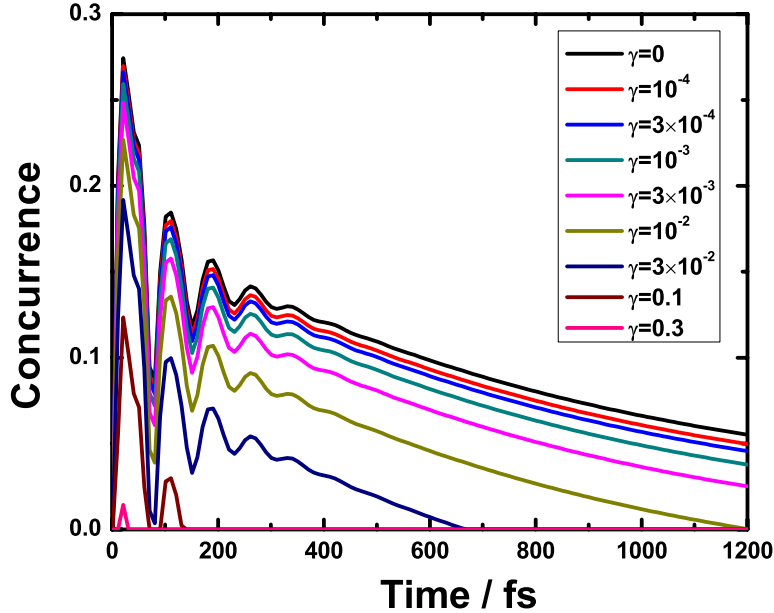


Figure 14: A comparison of the effects of adding in the two-exciton subspace $\gamma|\alpha|^2|0000011\rangle\langle 0000011|$ for different values of γ , with $|\alpha|^2 = 0.5$. The entanglement between sites one and two is plotted for the density matrix in 28, with $\rho_2 = |0000011\rangle\langle 0000011|$

V. CONCLUSIONS

In summary, we used the direct computation of the convex roof optimization approach to simulate the entanglement evolution in the FMO complex via the scaled HEOM approach. Our simulation results indicate the following results:

Pairwise entanglement plays the dominant role in entanglement of the FMO complex. Because of the saturation of the monogamy bounds the entanglement of any chromophore with any subset of the other chromophores is completely determined by the set of pairwise entanglements. For the simulations in which site 1 is initially excited, the dominant pair is site 1 and 2, while in the cases where 6 is initially excited site 5 and 6 are most entangled. This indicates that entanglement is dominant in the early stages of exciton transport, when the exciton is initially delocalized away from the injection site. In addition we observe that the entanglement mainly happens among the sites involved in the pathway. For the site 1 initially excited case, the entanglement of site 5, 6 and 7 is almost zero. For the site 6 initially excited situation, there is seldom entanglement for site 1 and 2.

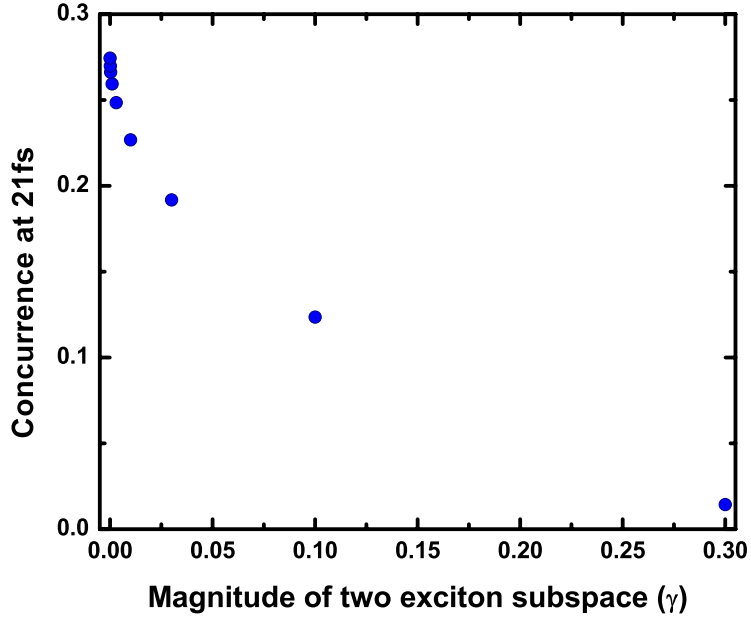


Figure 15: A curve showing how the amplitude of the entanglement between sites 1 and 2 at 21 fs varies as a function of γ , with the density matrix from 28, with $\rho_2 = |0000011\rangle\langle 0000011|$ and $|\alpha|^2 = .5$.

Although the final state is the same for both initial conditions, the role of site 3 and site 4 during the time evolution is different. For the initial condition where site 1 is excited, the entanglement is transferred to site 3 and then from site 3 to site 4. While for the site 6 initially excited case, sites 4 and 5 first become entangled with site 6 and then sites 3 and 4 become entangled. This is due to the fact that site 3 has strong coupling with site 1 and 2, while site 4 is coupled more strongly to sites 5, 6 and 7.

The initial condition plays an important role in the entanglement evolution, the entanglement decays faster for the cases where site 6 is initially excited compared with cases where the site 1 is initially excited. Increasing the temperature unsurprisingly reduces the amplitude of the entanglement and also decreases the time for the system goes to thermal equilibrium.

VI. FUTURE DIRECTIONS

Most entanglement measures computed previously for FMO were chosen on the basis of ease of calculation. The negativity and logarithmic negativity are straightforward to compute for all states [36, 46]. The global and bipartite relative entropy of entanglement can be made straightforward to compute by restriction to the single exciton subspace [42, 51]. The bipartite concurrence and tangles can be computed easily for pairs of chromophores [42, 47]. In all cases the chosen measures of simplifications thereof enable one to avoid computing the convex roof over different ensembles representing a mixed state. In this paper we explored the difficulty of such calculations, and find that measures that yield the bipartite entanglement across cuts of 3, 4, and 5 qubit subsystems may be computed with modest effort. We computed monogamy bounds, using the saturation of these bounds in the single exciton subspace [49] to evaluate the performance of our convex roof procedure. This technique enables us to extend the set of measures that have been computed for FMO, and also shows that the computation of entanglement for this system is not restricted by the difficulty of the convex roof procedure. This procedure could also be used, with no increase in computational cost, to analyze entanglement in multiexcitonic models.

VII. ACKNOWLEDGMENT

This Project is supported by NSF CCI center, "Quantum Information for Quantum Chemistry(QIQC)", Award number CHE-1037992, and by NSF award PHY-0955518.

-
- [1] Andrews, D. L.; Demidov, A. A. *Resonance Energy Transfer*; Wiley, 1999.
 - [2] Scholes, G. D. *J Phys Chem Lett* **2010**, *1*, 2–8.
 - [3] Scholes, G. D. *Nature Physics* **2010**, *6*, 402–403.
 - [4] Fenna, R. E.; Matthews, B. W. *Nature* **1975**, *258*, 573–577.
 - [5] Li, Y. F.; Zhou, W. L.; Blankenship, R. E.; Allen, J. P. *J Mol Biol* **1997**, *271*, 456–471.
 - [6] Camara-Artigas, A.; Blankenship, R. E.; Allen, J. P. *Photosynth Res* **2003**, *75*, 49–55.
 - [7] Cheng, Y. C.; Fleming, G. R. *Annu Rev Phys Chem* **2009**, *60*, 241–262.
 - [8] Engel, G. S.; Calhoun, T. R.; Read, E. L.; Ahn, T. K.; Mancal, T.; Cheng, Y. C.; Blankenship, R. E.; Fleming, G. R. *Nature* **2007**, *446*, 782–786.

- [9] Panitchayangkoon, G.; Hayes, D.; Fransted, K. A.; Caram, J. R.; Harel, E.; Wen, J.; Blanken-
ship, R. E.; Engel, G. S. *Proc Natl Acad Sci U S A* **2010**, *107*, 12766–70.
- [10] Mohseni, M.; Rebentrost, P.; Lloyd, S.; Aspuru-Guzik, A. *J Chem Phys* **2008**, *129*, 174106.
- [11] Rebentrost, P.; Mohseni, M.; Kassal, I.; Lloyd, S.; Aspuru-Guzik, A. *New J Phys* **2009**, *11*,
033003.
- [12] Rebentrost, P.; Mohseni, M.; Aspuru-Guzik, A. *J Phys Chem B* **2009**, *113*, 9942–9947.
- [13] Ishizaki, A.; Fleming, G. R. *J Chem Phys* **2009**, *130*, 234111.
- [14] Ishizaki, A.; Fleming, G. R. *Proc Natl Acad Sci U S A* **2009**, *106*, 17255–17260.
- [15] Zhu, J.; Kais, S.; Rebentrost, P.; Aspuru-Guzik, A. *J Phys Chem B* **2011**, *115*, 1531–1537.
- [16] Shi, Q.; Chen, L. P.; Nan, G. J.; Xu, R. X.; Yan, Y. J. *J Chem Phys* **2009**, *130*, 084105.
- [17] Rebentrost, P.; Aspuru-Guzik, A. *J Chem Phys* **2011**, *134*, 101103.
- [18] Kramer, T.; Kreisbeck, C.; Rodriguez, M.; Hein, B. **2011**, American Physical Society March
Meeting.
- [19] Berkelbach, T. C.; Markland, T. E.; Reichman, D. R. *arXiv: 1111.5026v1* **2011**,
- [20] Prior, J.; Chin, A. W.; Huelga, S. F.; Plenio, M. B. *Phys Rev Lett* **2010**, *105*, 050404.
- [21] Huo, P.; Coker, D. F. *J Chem Phys* **2010**, *133*, 184108.
- [22] Moix, J.; Wu, J.; Huo, P.; Coker, D.; Cao, J. *J Phys Chem Lett* **2011**, *2*, 3045–3052.
- [23] Skochdopole, N.; Mazziotti, D. A. *J Phys Chem Lett* **2011**, *2*, 2989–2993.
- [24] Mazziotti, D. A. *arXiv: 1112.5863v1* **2011**,
- [25] Nalbach, P.; Braun, D.; Thorwart, M. *Phys Rev E* **2011**, *84*, 041926.
- [26] Shabani, A.; Mohseni, M.; Rabitz, H.; Lloyd, S. *arXiv: 1103.3823v3* **2011**,
- [27] Mohseni, M.; Shabani, A.; Lloyd, S.; Rabitz, H. *arXiv: 1104.4812v1* **2011**,
- [28] Lloyd, S.; Mohseni, M.; Shabani, A.; Rabitz, H. *arXiv:1111.4982v1* **2011**,
- [29] Kim, J. H.; Cao, J. S. *J Phys Chem B* **2010**, *114*, 16189–16197.
- [30] Wu, J.; Liu, F.; Ma, J.; Silbey, R. J.; Cao, J. *arXiv:1109.5769v1* **2011**,
- [31] Wu, J. L.; Liu, F.; Shen, Y.; Cao, J. S.; Silbey, R. J. *New J Phys* **2010**, *12*, 105012.
- [32] Vlaming, S. M.; Silbey, R. J. *arXiv: 1111.3627v1* **2011**,
- [33] Renaud, N.; Ratner, M. A.; Mujica, V. *J Chem Phys* **2011**, *135*, 075102.
- [34] Abramavicius, D.; Mukamel, S. *J Chem Phys* **2010**, *133*, 064510.
- [35] Kais, S. *Entanglement, Electron Correlation and Density matrices, in Reduced-Density-Matrix
Mechanics - with Application to Many-Electron Atoms and Molecules (John Wiley & Sons Inc,
New York, 2007) Vol. 134 of Adv. Chem. Phys., pp. 493–535.*
- [36] Thorwart, M.; Eckel, J.; Reina, J. H.; Nalbach, P.; Weiss, S. *Chem Phys Lett* **2009**, *478*, 234.

- [37] Peres, A. *Phys Rev Lett* **1996**, *77*, 1413.
- [38] Horodecki, M.; Horodecki, P.; Horodecki, R. *Phys Lett A* **1996**, *223*, 1.
- [39] Whaley, K. B.; Sarovar, M.; Ishizaki, A. *arXiv: 1012.4059v1* **2010**, *quant-ph*.
- [40] Mukamel, S. *J Chem Phys* **2010**, *132*, 241105.
- [41] Panitchayangkoon, G.; Voronine, D. V.; Abramavicius, D.; Caram, J. R.; Lewis, N. H. C.; Mukamel, S.; Engel, G. S. *Proc Natl Acad Sci U S A* **2011**, *108*, 20908–20912.
- [42] Sarovar, M.; Ishizaki, A.; Fleming, G. R.; Whaley, K. B. *Nature Physics* **2010**, *6*, 462 – 467.
- [43] Wootters, W. *Phys Rev Lett* **1998**, *80*, 2245–2248.
- [44] Plenio, M. B. *Phys Rev Lett* **2005**, *95*, 090503.
- [45] Caruso, F.; Chin, A. W.; Datta, A.; Huelga, S. F.; Plenio, M. B. *Phys Rev A* **2010**, *81*, 62346.
- [46] Caruso, F.; Chin, A. W.; Datta, A.; Huelga, S. F.; Plenio, M. B. *J Chem Phys* **2009**, *131*, 5106.
- [47] Fassioli, F.; Olaya-Castro, A. *New J Phys* **2010**, *12*, 085006.
- [48] Meyer, D. A.; Wallach, N. R. *arXiv: 0108104v1* **2001**, *quant-ph*.
- [49] Kim, J. S.; Sanders, B. C. *J Phys A* **2008**, *41*, 5301.
- [50] Meier, T.; Chernyak, V.; Mukamel, S. *J Phys Chem B* **1997**, *101*, 7332–7342.
- [51] Bradler, K.; Wilde, M. M.; Vinjanampathy, S.; Uskov, D. B. *Phys Rev A* **2010**, *82*, 062310.
- [52] Tanimura, Y. *J Phys Soc Jpn* **2006**, *75*, 082001.
- [53] Ishizaki, A.; Tanimura, Y. *J Phys Soc Jpn* **2005**, *74*, 3131–3134.
- [54] Love, P. J.; Brink, A. M.; Smirnov, A. Y.; Amin, M. H. S.; Grajcar, M.; Il'ichev, E.; Iz-malkov, A.; Zagoskin, A. M. *Quantum Inf Process* **2007**, *6*, 187–195.
- [55] Brennen, G. K. *Quantum Inf Comput* **2003**, *3*, 619.
- [56] Scott, A. *Phys Rev A* **2004**, *69*, 052330.
- [57] Yu, C.-S.; Song, H.-S. *Phys Rev A* **2006**, *73*, 022325.
- [58] Coffman, V.; Kundu, J.; Wootters, W. K. *Phys Rev A* **2000**, *61*, 52306.
- [59] Osborne, T.; Verstraete, F. *Phys Rev Lett* **2006**, *96*, 220503.
- [60] Ou, Y.-C. *arXiv: 0612127v3* **2006**, *quant-ph*.
- [61] Kirkpatrick, K. *Foundations of Physics Letters* **2006**, *19*, 95–102.
- [62] Cayley, A. *Journal für die Reine und Angewandte Mathematik* **1846**, *32*, 119–123, Republished in Cayley, Arthur (1889), "The Collected Mathematical Papers of Arthur Cayley," Cambridge University Press.
- [63] Röthlisberger, B.; Lehmann, J.; Loss, D. *Phys Rev A* **2009**, *80*, 042301.
- [64] Życzkowski, K. *Phys Rev A* **1999**, *60*, 3496.